New insight into the massive eccentric binary HD 165052*: self-consistent orbital solution, apsidal motion, and fundamental parameters

S. Rosu[1,2]†, E. A. Quintero[3,4], G. Rauw[2], and P. Eenens[3]

[1]*Department of Physics, KTH Royal Institute of Technology, The Oskar Klein Centre, AlbaNova, SE-106 91 Stockholm, Sweden*
[2]*Space sciences, Technologies and Astrophysics Research (STAR) Institute, Université de Liège, Allée du 6 Août, 19c, Bât B5c, 4000 Liège, Belgium*
[3]*Departamento de Astronomía, Universidad de Guanajuato, Guanajuato, Mexico*
[4]*Observatorio Astronómico (OAUTP), Universidad Tecnológica de Pereira, Risaralda, Colombia*

ABSTRACT

HD 165052 is a short-period massive eccentric binary system that undergoes apsidal motion. As the rate of apsidal motion is directly related to the internal structure constants of the binary components, its study allows to get insight into the internal structure of the stars. We use medium- and high-resolution spectroscopic observations of HD 165052 to provide constraints on the fundamental properties of the binary system and the evolutionary state of its components. We apply a spectral disentangling code to reconstruct artefact-free spectra of the individual stars and derive the radial velocities (RVs) at the times of the observations. We perform the first analysis of the disentangled spectra with the non-LTE model atmosphere code CMFGEN to determine the stellar properties. We derive the first self-consistent orbital solution of all existing RV data, including those reported in the literature, accounting for apsidal motion. We build, for the very first time, dedicated stellar evolution tracks with the Clés code requesting the theoretical effective temperatures and luminosities to match those obtained from our spectroscopic analysis. The binary system HD 165052, consisting of an O6.5 V((f)) primary ($T_{\rm eff,P}$ = 37 500 ± 1000 K) and an O7 V((f)) secondary ($T_{\rm eff,S}$ = 36 000 ± 1000 K), displays apsidal motion at a rate of $(11.30^{+0.64}_{-0.49})°\,{\rm yr}^{-1}$. Evolutionary masses are compared to minimum dynamical masses to constrain the orbital inclination. Evolutionary masses $M_{\rm ev,P}$ = 24.8 ± 1.0 $M_\odot$ and $M_{\rm ev,S}$ = 20.9 ± 1.0 $M_\odot$ and radii $R_{\rm ev,P}$ = $7.0^{+0.5}_{-0.4}\,R_\odot$ and $R_{\rm ev,S}$ = $6.2^{+0.4}_{-0.3}\,R_\odot$ are derived, and the inclination is constrained to $22.1° \leq i \leq 23.3°$. Theoretical apsidal motion rates, derived assuming an age of 2.0 ± 0.5 Myr for the binary, are in agreement with the observational determination. The agreement with theoretical apsidal motion rates enforces the inferred values of the evolutionary stellar masses and radii.

Key words: stars: early-type – stars: evolution – stars: individual (HD 165052) – stars: massive – binaries: spectroscopic

1 INTRODUCTION

Massive stars play a key role in many processes in the Universe, notably through their winds and powerful supernova explosions that contribute to the chemical enrichment of the Universe. It is nowadays thought that the majority of the massive stars (i.e. O and B-type stars having a mass larger than 8 $M_\odot$) are, or have been, part of a binary or higher multiplicity system (Duchêne & Kraus 2013). According to current estimates, more than 70% of the massive stars inhabiting our Galaxy have spent some part of their existence in a binary system (Sana et al. 2012). The simple fact of being bound to another star by gravitational attraction can deeply modify the evolutionary track of the considered star, as its evolution is now driven not only by its own properties – initial mass, mass-loss rate (a problem that has not been self-consistently solved in stellar structure and evolution models yet), and rotation rate (Ekström et al. 2012; Brott et al. 2011) –, but also by the binary orbit's parameters (e.g., Wellstein et al. 2001). The

study of detached eclipsing and/or spectroscopic binaries is the most accurate way to obtain reliable physical properties of O and B stars. Among these systems, those showing evidence for apsidal motion (i.e. slow precession of the binary system major axis) offer additional possibilities to sound the interior of these massive stars. Indeed, the apsidal motion rate is directly related to the internal structure constant of the stars that make up the binary system (Shakura 1985). The internal structure constant is a sensitive indicator of the density stratification inside a star and its value strongly changes as the star evolves away from the main sequence. Measuring the rate of apsidal motion in a binary system hence not only provides a diagnostic of the – otherwise difficult to constrain – internal structure of the stars, but also offers a test of our understanding of stellar structure and evolution (Claret & Giménez 2010; Mazeh 2008).

The massive eccentric binary HD 165052 is a well-known early-type double-lined spectroscopic (SB2) binary system of the very young open cluster NGC 6530. NGC 6530 is itself located in the centre of the H II region M8, also known as the Lagoon Nebula. This cluster is one of the most studied clusters in our Galaxy, notably for its interesting history of ongoing star formation (Sung et al. 2000; Arias et al. 2002). The age of NGC 6530 was estimated by

---

Table 1. Physical and orbital parameters of HD 165052 from the literature.

Reference Parameter	Stickland et al. (1997)	Arias et al. (2002)	Linder et al. (2007)	Ferrero et al. (2013)
			Value	
Spectral type	...	O6.5 V + O7.5 V	O6 V + O6.5 V	O7 Vz + O7.5 Vz
P_{orb} (d)	2.955055 ± 0.000010	2.95510 ± 0.00001	2.95515 ± 0.00004	2.95506 ± 0.00002
e	0 (fixed)	0.090 ± 0.004	0.081 ± 0.015	0.090 ± 0.003
K_P (km s^{-1})	95.6 ± 2.2	94.8 ± 0.5	96.4 ± 1.6	97.4 ± 0.4
K_S (km s^{-1})	109.6 ± 2.2	104.7 ± 0.5	113.5 ± 1.9	106.5 ± 0.4
i (°)	18.7 ± 0.4 (approx.)	...	...	...
$a_P \sin i$ ($R_\odot$)	5.58 ± 0.13	5.51 ± 0.03	5.6 ± 0.1	5.66 ± 0.03
$a_S \sin i$ ($R_\odot$)	6.40 ± 0.13	6.09 ± 0.03	6.6 ± 0.1	6.20 ± 0.03
$M_P \sin^3 i$ ($M_\odot$)	2.23 ± 0.06	1.26 ± 0.03	1.5 ± 0.1	1.34 ± 0.03
$M_S \sin^3 i$ ($M_\odot$)	1.41 ± 0.07	1.14 ± 0.03	1.3 ± 0.1	1.22 ± 0.03
$q = M_S/M_P$	0.873 ± 0.027	0.90 ± 0.01	0.85 ± 0.01	0.91 ± 0.01
R_P ($R_\odot$)	15.5 ± 1.5	...	...	...
R_S ($R_\odot$)	14.6 ± 1.1	...	...	...

The parameters are the following: P_{orb}, the orbital period of the system; e, the eccentricity of the orbit; K_P (respectively K_S), the amplitude of the RV curve of the primary (respectively secondary) star; i, the orbital inclination; $a_P \sin i$ (respectively $a_S \sin i$), the projected semi-major axis of the primary (respectively secondary) orbit; $M_P \sin^3 i$ (respectively $M_S \sin^3 i$), the minimum mass of the primary (respectively secondary) star; $q = M_S/M_P$, the mass ratio of the system; and R_P (respectively R_S), the radius of the primary (respectively secondary) star. The errors represent $\pm 1\sigma$.

several authors (we refer to Ferrero et al. 2013, for a critical discussion). Most authors agree about an age estimate around 2 Myr: van Altena & Jones (1972) and Mayne & Naylor (2008) both derived an age of 2 Myr, Sagar & Joshi (1978) set a lower limit of 2 Myr though star formation would have continued as recently as 0.25 Myr ago, Kilambi (1977) estimated the age to range from 1 to 3 Myr, Sung et al. (2000) estimated the age to 1.5 Myr with an age spread of 4 Myr, Damiani et al. (2004) derived a median age of cluster stars in the central region of 0.8 Myr, with a maximum age spread for the whole NGC 6530 cluster of 4 Myr, and Prisinzano et al. (2005) derived an age of 2.3 Myr with an age spread compatible with 2 Myr. Only Böhm-Vitense et al. (1984) derived a much larger age of 5 ± 2 Myr.

Plaskett (1924) was the first to report evidence for binarity of HD 165052 through the discovery of a variable radial velocity (RV). Conti (1974) pointed out the double-lined binary nature of HD 165052. The very first orbital solution was proposed by Morrison & Conti (1978). However, due to the apparent similarity in the optical region between the two components of the binary, the authors did not unambiguously identify the two components and derived an orbital period of 6.14 days that appeared to be erroneous. Stickland et al. (1997) revisited the orbital period P_{orb} = 2.96 days of the system, among other properties (see Table 1), based on 15 high-resolution *IUE* spectra. The binary system was classified as O6.5 V + O6.5 V by Walborn (1972), modified to O6.5 V(n)((f)) + O6.5 V(n)((f)) by Walborn (1973), and to O6 V + O6 V by Penny (1996). Arias et al. (2002) presented a new optical spectroscopic study of HD 165052 based on intermediate and high-resolution CCD observations. The authors derived a new orbital solution for the system (see Table 1) and found, for the first time, evidence of apsidal motion in the system from the comparison with previous RV determinations (Arias et al. 2002). Linder et al. (2007) investigated the Struve-Sahade effect that was originally pointed out in the system by Arias et al. (2002) and also derived a new orbital solution for the system (see Table 1). Finally, Ferrero et al. (2013) presented a new set of RV measurements of HD 165052 which they obtained through the disentangling of high-resolution optical spectra using the method described by González & Levato (2006). They provided a new orbital solution for the system (see Table 1) and confirmed the variation of the longitude of periastron with time. The authors

derived the first estimate of the apsidal motion rate in the system: $\dot\omega = (12.1 \pm 0.3)° \text{yr}^{-1}$.

In this article, we perform a new, in-depth spectroscopic investigation of the binary HD 165052 through the analysis of both old and new medium- and high-resolution spectra. We reassess the fundamental and orbital parameters of the system making use of the most advanced disentangling method proposed by Quintero et al. (2020) that allows the reconstruction of artefact-free individual spectra. We further analyse those reconstructed spectra with, for the first time, a non-LTE model atmosphere code, namely CMFGEN. We derive the first self-consistent orbital solution of all existing RV data, including those reported in the literature, accounting for the change of the longitude of periastron with time. Given that the rate of apsidal motion is directly related to the internal stellar structure constants of the binary components, its determination allows us to infer additional constraints to perform critical tests of stellar structure and evolution models (Claret & Torres 2019; Claret et al. 2021, and references therein). Finally, we also compute dedicated stellar structure and evolution tracks to derive evolutionary masses and radii for the stars and to put a robust constraint on the value of the inclination of the orbit, as well as to see how the theoretical apsidal motion rates compare to the observational value.

The set of spectroscopic data we use is introduced in Sect. 2. In Sect. 3 we perform the spectral disentangling, reassess the spectral classification of the stars, and analyse the reconstructed spectra by means of the CMFGEN non-LTE model atmosphere code (Hillier & Miller 1998). The RVs deduced from the spectral disentangling are combined with data from the literature in Sect. 4 to derive values for the orbital period, the mass ratio, the rate of apsidal motion, and the orbital eccentricity of the system, among others. The stellar structure and evolution tracks computed with the Code Liégeois d'Évolution Stellaire are presented in Sect. 5. We provide our conclusions in Sect. 6.

2 OBSERVATIONAL DATA

2.1 Spectroscopy

We extracted a total of 47 medium- and high-resolution échelle spectra of HD 165052 in the optical domain from the ESO science archive.

Those spectra were collected between May 1999 and July 2017 using different instruments. Twenty-one spectra were obtained with the Fiber-fed Extended Range Optical Spectrograph (FEROS) mounted on the European Southern Observatory (ESO) 1.5 m telescope in La Silla, Chile (Kaufer et al. 1999), between May 1999 and April 2002, three spectra were obtained with the FEROS instrument mounted on the ESO 2.2 m telescope between May 2004 and April 2007. FEROS has a spectral resolving power of 48 000. The FEROS data were reduced using the FEROS pipeline of the MIDAS software. Ten spectra were obtained with the ESPaDOnS spectrograph attached to the Canada-France-Hawaï observatory (CFH) 3.6 m telescope in Hawaï (Donati et al. 2003). These data were collected during a single night in June 2010. ESPaDOnS has a spectral resolving power of 68 000. The reduced ESPaDOnS data were retrieved from the CFHT archive. Four spectra were obtained with the Ultraviolet and Visual Echelle Spectrograph (UVES) mounted on the ESO Very Large Telescope (VLT) at Cerro Paranal, Chile (Dekker et al. 2000), during a single night in November 2002. UVES has a spectral resolving power of 65 030 in the blue arm and of 74 450 in the red arm. The wavelength domain ranges from 3000 to 5000 (blue arm) and from 4200 to 11 000 (red arm). Nine spectra were obtained with the XSHOOTER instrument mounted on the VLT (Vernet et al. 2011), in July 2016 and July 2017. The wavelength domain ranges from 3000 to 5595 (UVB) and from 5595 to 10 240 (VIS). The spectral resolving power of XSHOOTER is, depending on the observations, 4112 or 5453 (UVB) and 6505, 8935, or 11 333 (VIS). The ESPaDOnS, UVES, and XSHOOTER spectra provided in the archive were already reduced using the dedicated pipelines. We complemented those spectra with 24 high-resolution échelle spectra obtained with the HEROS instrument mounted on the TIGRE telescope between April 2019 and April 2021 (González-Pérez et al. 2022). The wavelength domain ranges from 3500 to 5600 (blue channel) and from 5800 to 8800 (red channel). The spectral resolving power is 20 000. For all the spectra, we removed cosmic rays and telluric absorption lines using MIDAS and the telluric tool within IRAF, respectively. We normalised the spectra with MIDAS by fitting low-order polynomials to the continuum as in Rosu et al. (2020b, 2022a,b). The journal of the spectroscopic observations is presented in Table A1, together with the radial velocities computed in Sect. 3.1 and the phase computed using the orbital period derived in Sect. 4.

3 SPECTRAL ANALYSIS

3.1 Spectral disentangling

As a first step, we performed the spectral disentangling of all data using our disentangling code based on the method described by González & Levato (2006). We derived the individual spectra of the binary components as well as their RVs at the times of the observations. We refer to González & Levato (2006), Marchenko et al. (1998), and Quintero et al. (2020) for detailed information about the methodology and its limitations, and to Appendix A for a detailed description of the method adopted in the present context.

The resulting RVs of both stars are reported in Table A1 together with their 1σ errors.

We confirm the observations of Ferrero et al. (2013) who reported artefacts in the spectra of the stellar components of HD 165052 after disentangling using the version of the "shift and add" technique of Marchenko et al. (1998), a precursor of the code proposed by González & Levato (2006). Quintero et al. (2020) demonstrated that the shift and add method produces artefacts when the spectra contain
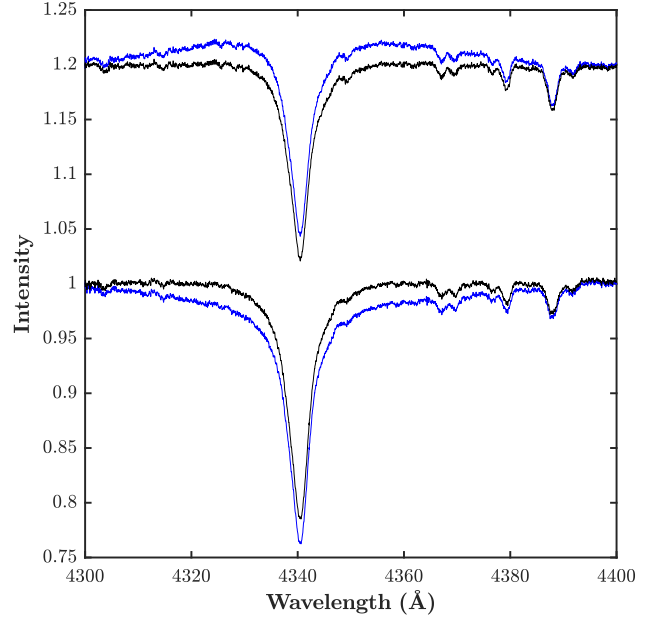

Figure 1. Reconstructed spectra of the stellar components of HD 165052 in the wavelength domain around the Hγ line, using the shift and add method (blue) and the QER20 Package (black). The spectra of the stellar components are vertically shifted for clarity.

broad lines with low Doppler shifts. These artefacts distort the spectral line profiles, producing uncertainties in the flux and the profile of the spectral lines of the stellar components.

The novel QER20 spectral disentangling algorithm proposed by Quintero et al. (2020) combines the advantages of the shift and add method (versatility and ease of implementation) with artefact-free reconstructed spectra. The fundamental principle of the QER20 Package consists in considering the integrated flux of a given spectral line as a free parameter (see Quintero et al. 2020, for a detailed description of the QER20 algorithm).

Hence, as a second step, we used the QER20 algorithm, fixing the RVs of the stars to those computed previously and reported in Table A1. In order to illustrate the reliability of this novel disentangling method in the case of the binary HD 165052, Figure 1 compares the reconstructed Hγ line of both stellar components, obtained with the shift and add method and the QER20 Package. The former shows the artefacts mentioned above: emission wings in the spectrum of the primary, and absorption wings in the secondary. In contrast, the QER20 Package yields profiles free of these artefacts. The difference in integrated flux of the lines amounts to 5% to 7% between the two methods.

3.2 Spectral classification and absolute magnitudes

We reassessed the spectral classification of the binary components of HD 165052 based on their reconstructed spectra.

To determine the spectral types of the stars, we used Conti's criterion (Conti & Alschuler 1971) complemented by Mathys (1988). We found that $\log W' = \log[\text{EW}(\text{He\,\textsc{i}}\ \lambda\,4471)/\text{EW}(\text{He\,\textsc{ii}}\ \lambda\,4542)]$ amounts to -0.17 ± 0.01 for the primary star and to -0.05 ± 0.01 for the secondary star, which correspond to spectral types O6.5 and O7 (with spectral type O7.5 within the error bars), respectively. We also followed the Walborn criterion (Walborn & Fitzpatrick 1990) based on the strengths of the He\,\textsc{ii}\ $\lambda\,4686$ line and the N\,\textsc{iii}\ $\lambda\lambda\,4634$-40-42

triplet to asses the luminosity classes of the stars. Given that He II λ 4686 is seen in strong absorption and N III $\lambda\lambda$ 4634-40-42 in weak absorption, both stars are of luminosity class V((f)).

We estimated the brightness ratio of HD 165052 in the visible domain based on the ratio between the equivalent widths (EWs) of the spectral lines of the secondary star and TLUSTY spectra of similar effective temperatures. We used the Hβ, Hγ, He I $\lambda\lambda$ 4026, 4471, 5016, and He II λ 4542 lines. The ratio EW$_{\text{TLUSTY}}$/EW$_{\text{sec}}$ = $(l_P + l_S)/l_S$ amounts to 2.42 ± 0.39 and 2.43 ± 0.37 when TLUSTY spectra of T_{eff} of 37 500 and 35 000 K, respectively, are used. Both results give us $l_S/l_P = 0.70 \pm 0.19$.

Bailer-Jones et al. (2021) derived a distance of $1212.7^{+42.8}_{-31.5}$ pc from the parallax of $\varpi = 0.7893 \pm 0.0297$ mas quoted by *Gaia* early data release 3 (EDR3, Gaia Collaboration 2021). This leads to a distance modulus of $10.42^{+0.08}_{-0.06}$ for the binary system. Mean V and B magnitudes of 6.87 and 6.98, respectively, are reported by Zacharias et al. (2013), for which we estimated errors of 0.01. We adopted a value of -0.27 ± 0.01 for the intrinsic colour index $(B-V)_0$ of an O6.5-O7 V star (Martins & Plez 2006) and assumed the reddening factor in the V-band R_V equal to 3.15 ± 0.06 for NGC 6530 (Topasna et al. 2020). In this way, we obtained an absolute magnitude in the V-band of the binary system $M_V = -4.75^{+0.10}_{-0.08}$. Using the brightness ratio, we then derived individual absolute magnitudes $M_{V,P} = -4.17 \pm 0.15$ and $M_{V,S} = -3.79^{+0.20}_{-0.19}$ for the primary and secondary stars, respectively.

From the comparison with the magnitudes reported by Martins & Plez (2006), we observe that the primary star is slightly less luminous than a 'typical' O6.5 V star while the secondary star is fainter than expected for O7-O7.5 V type stars.

3.3 Projected rotational velocities

We used the Fourier transform method (Simón-Díaz & Herrero 2007; Gray 2008) and proceeded as in Rosu et al. (2022a) to derive the projected rotational velocities of both stars. The results are summarised in Table 2, and the Fourier transforms of the C IV λ 5801 line for the primary star and of the Si IV λ 4631 line for the secondary star are illustrated in Fig. 2. The results presented in Table 2 show that the mean $v \sin i_{\text{rot}}$ computed on metallic lines alone or on all the lines agree very well. We adopted a mean $v \sin i_{\text{rot}}$ of 67 ± 8 km s^{-1} for the primary star and of 62 ± 7 km s^{-1} for the secondary star. Our values are compatible, within the error bars, with those derived by Morrison & Conti (1978), Stickland et al. (1997), Linder et al. (2007), and Ferrero et al. (2013) but are slightly lower than those quoted by Howarth et al. (1997).

3.4 Model atmosphere fitting

We analysed the reconstructed spectra of the binary components by means of the non-LTE model atmosphere code CMFGEN (Hillier & Miller 1998) to constrain the fundamental properties of the stars. We broadened the CMFGEN spectra by the projected rotational velocities determined in Sect. 3.3 and adjusted the stellar and wind parameters following the procedure outlined by Martins (2011).

Given that the surface gravity derived in the CMFGEN adjustment is underestimated for a binary star (Palate & Rauw 2012), we decided to fix the value of the surface gravity log g_{spectro} to 3.92 cgs for both stars following Tables 1 and 4 in Martins et al. (2005). We fixed the microturbulence value at the level of the photosphere, $v_{\text{micro}}^{\text{min}}$, to 15 km s^{-1}. The clumping parameters of the wind were fixed: the

Table 2. Best-fit projected rotational velocities as derived from the disentangled spectra of HD 165052 and comparison with results coming from the literature.

Line	$v \sin i_{\text{rot}}$ (km s^{-1})	
	Primary	Secondary
Si IV λ 4089	75	56
Si IV λ 4116	...	59
Si IV λ 4212	66	...
Si IV λ 4631	55	73
O III λ 5592	73	59
C IV λ 5801	64	...
C IV λ 5812	...	61
He I λ 3820	79	...
He I λ 4120	...	73
He I λ 4143	74	...
He I λ 4387	73	77
He I λ 4471	...	73
He I λ 4922	...	57
He I λ 5016	73	...
He I λ 5876	...	62
Mean (metallic lines)	67 ± 8	62 ± 7
Mean (He I lines)	75 ± 3	68 ± 8
Mean (all lines)	70 ± 7	65 ± 8
Stickland et al. (1997)	85 ± 8	80 ± 6
Howarth et al. (1997)	91	78
Linder et al. (2007)	73 ± 7	80 ± 7
Ferrero et al. (2013)	71 ± 5	66 ± 5

The values quoted by Stickland et al. (1997) and Howarth et al. (1997) were obtained by cross-correlation techniques applied to *IUE* spectra. The values quoted by Linder et al. (2007) were obtained by applying the Fourier method (see Simón-Díaz & Herrero 2007; Gray 2005) to the profiles of their disentangled He I λ 4471, He II λ 4542, and Hβ line profiles. The values quoted by Ferrero et al. (2013) were obtained using their empirical regressions between the full widths at half-maximum of intensity and $v \sin i_{\text{rot}}$ values derived based on the convolution of the spectrum of τ Sco with rotation-line profiles.

volume filling factor f_1 was set to 0.1, and the f_2 parameter controlling the onset of clumping was set to 100 km s^{-1}, as in Rosu et al. (2020b). Likewise, the β parameter of the velocity law was fixed to 1.0 as suggested by Muijres et al. (2012) for O6.5-O7 V type stars. The wind terminal velocity v_∞ was fixed to 2335 km s^{-1} for both stars, as derived from the combined *IUE* spectra by Howarth et al. (1997).

We adjusted the macroturbulence velocity v_{macro} on the wings of the O III λ 5592 and Balmer lines and derived values of 120 ± 20 km s^{-1} and 65 ± 10 km s^{-1} for the primary and secondary stars, respectively.

The stellar and wind parameters of the best-fit CMFGEN model atmosphere are summarised in Table 3. The normalised disentangled spectra of HD 165052 are illustrated in Fig. 3 along with the best-fit CMFGEN adjustments.

We derived the effective temperature based on the adjustment of the He I $\lambda\lambda$ 4121, 4471, 4713, 4922, 5016, 5874, 7065 and He II $\lambda\lambda$ 4200, 4542, 5412 lines. This was clearly a compromise as we could not find a solution that perfectly fits all helium lines simultaneously. We discarded the He I λ 4026 line because of its blend with the weak but non-zero He II λ 4026 line. We derived effective temperatures $T_{\text{eff,1}} = 37\,500 \pm 1000$ K and $T_{\text{eff,2}} = 36\,000 \pm 1000$ K for the primary and secondary stars, respectively.

The mass-loss rate was derived based on the adjustment of the Hα and He II λ 4686 lines. We derived values of $(1.5 \pm 0.5) \times$
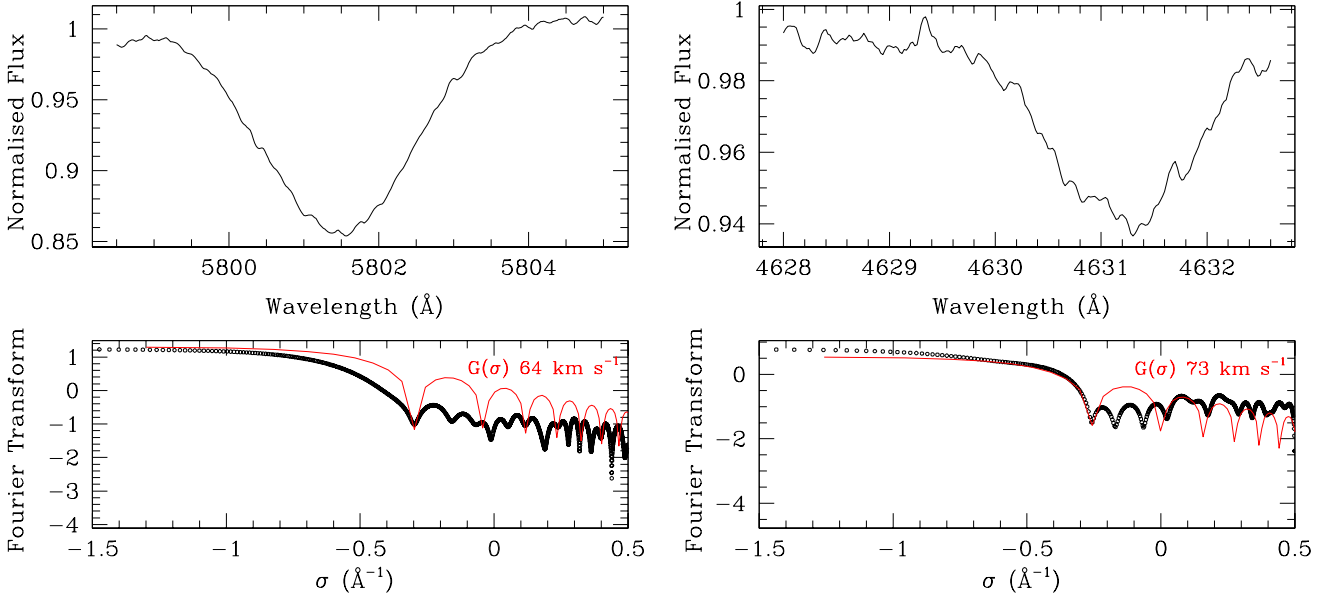
Figure 2. Fourier transforms of primary and secondary lines. *Top row:* Line profiles of the separated spectra of HD 165052 obtained after application of the brightness ratio for the primary (C IV λ 5801 line, *left panel*) and secondary (Si IV λ 4631 line, *right panel*) stars. *Bottom row:* Fourier transform of those lines (in black) and best-match rotational profile (in red) for the primary (*left panel*) and secondary (*right panel*) stars.

10^{-7} $M_\odot$ yr^{-1} and $(9.0 \pm 1.0) \times 10^{-8}$ $M_\odot$ yr^{-1} for the primary and secondary stars, respectively.

We set the surface chemical abundances of all elements, including helium, but excluding carbon and oxygen, to solar as taken from Asplund et al. (2009). We derived the oxygen abundance based on the O III λ 5592 line as it is the sole oxygen line free of blends. We derived sub-solar oxygen abundances in number O/H of $(3.0 \pm 0.2) \times 10^{-4}$ and $(4.0 \pm 0.2) \times 10^{-4}$ for the primary and secondary stars, respectively. For both stars, with these oxygen abundances, the weak O III $\lambda\lambda$ 4368, 4448, 4454, 4458 lines are well-reproduced, while the O III λ 5508 line is slightly overestimated. We derived the carbon abundance based on the C III λ 4070 line as it is the sole reliable carbon line free of blends. Indeed, as stated by Martins & Hillier (2012), the C III $\lambda\lambda$ 4647-51 blend and the C III λ 5696 line are known to be problematic because their formation processes are controlled by a number of far-UV lines, hence their strength and nature critically depend upon subtle details of the stellar atmosphere model. The C III λ 4379 line is heavily blended with the N III λ 4379 and therefore useless, while the C III λ 4388 line is not significantly affected by a change in carbon abundance. We also know the C IV λ 5801, 5812 lines to be problematic and rarely correctly reproduced (Rosu et al. 2020b). We derived a sub-solar carbon abundances in number C/H of $(2.0 \pm 0.2) \times 10^{-4}$ for both stars. Finally, we set the nitrogen abundance to solar as taken from Asplund et al. (2009) as we could not adjust the nitrogen abundance based on the nitrogen lines. Indeed, N III λ 4379 is heavily blended with C III λ 4379, the N III $\lambda\lambda$ 4510-4540 blend is not significantly affected by a change in nitrogen abundance, and the CMFGEN spectra display the N III $\lambda\lambda$ 4634-4640 complex in emission. We tested a nitrogen abundance 4.83 (respectively 3.35) times solar for the primary (respectively secondary) star – such that, combined with the depleted C and O abundances, the CNO abundance is solar – and observed that the nitrogen lines in the CMFGEN spectra were much deeper than in the observational spectra. This results suggests that the initial metallicity of the stars is (at least slightly) sub-solar.

We computed the bolometric magnitudes of the stars assuming the bolometric correction depends only on the effective temperature

Table 3. Stellar and wind parameters of the best-fit CMFGEN model atmosphere derived from the separated spectra of HD 165052.

Parameter	Value	
	Primary	Secondary
$T_{\rm eff}$ (K)	$37\,500 \pm 1000$	$36\,000 \pm 1000$
$\log g_{\rm spectro}$ (cgs)	3.92 (fixed)	3.92 (fixed)
$v_{\rm macro}$ (km s^{-1})	120 ± 20	65 ± 10
$v_{\rm micro}^{\rm min}$ (km s^{-1})	15 (fixed)	15 (fixed)
$\dot{M}$ ($M_\odot$ yr^{-1})	$(1.5 \pm 0.5) \times 10^{-7}$	$(9.0 \pm 1.0) \times 10^{-8}$
$\dot{M}_{\rm uncl.}$ ($M_\odot$ yr^{-1})[a]	$(4.7 \pm 1.6) \times 10^{-7}$	$(2.8 \pm 0.3) \times 10^{-7}$
v_∞ (km s^{-1})	2335 (fixed)	2335 (fixed)
f_1	0.1 (fixed)	0.1 (fixed)
f_2 (km s^{-1})	100 (fixed)	100 (fixed)
β	1.1 (fixed)	1.1 (fixed)
He/H (nb)	0.0851^b (fixed)	0.0851^b (fixed)
C/H (nb)	$(2.0 \pm 0.2) \times 10^{-4}$	$(2.0 \pm 0.2) \times 10^{-4}$
N/H (nb)	6.76×10^{-5} (fixed^b)	6.76×10^{-5} (fixed^b)
O/H (nb)	$(3.0 \pm 0.2) \times 10^{-4}$	$(4.0 \pm 0.2) \times 10^{-4}$

[a] $\dot{M}_{\rm uncl.} = \dot{M}/\sqrt{f_1}$ is the unclumped mass-loss rate.
[b] Value fixed to the solar chemical abundance (Asplund et al. 2009).

through the relation

$$BC = -6.89 \log(T_{\rm eff}) + 28.07 \qquad (1)$$

(Martins & Plez 2006) and got $M_{\rm bol,P} = -7.61 \pm 0.17$ and $M_{\rm bol,S} = -7.11 \pm 0.21$, which then converted into bolometric luminosities give us $L_{\rm bol,P} = 89\,000 \pm 14\,000\,L_\odot$ and $L_{\rm bol,S} = 56\,000 \pm 11\,000\,L_\odot$. Combined with the effective temperatures derived from the CMFGEN analysis, we inferred spectroscopic radii $R_{\rm spectro,P} = 7.1 \pm 0.7\,R_\odot$ and $R_{\rm spectro,S} = 6.1 \pm 0.7\,R_\odot$. The surface gravities, corrected for both the centrifugal force and radiation pressure, amount to 3.99 ± 0.01 and $3.98^{+0.02}_{-0.01}$ for the primary and secondary stars, respectively. Spectroscopic masses $M_{\rm spectro,P} = 17.7^{+3.5}_{-3.4}\,M_\odot$ and $M_{\rm spectro,S} = 12.9 \pm 2.9\,M_\odot$ were then inferred.
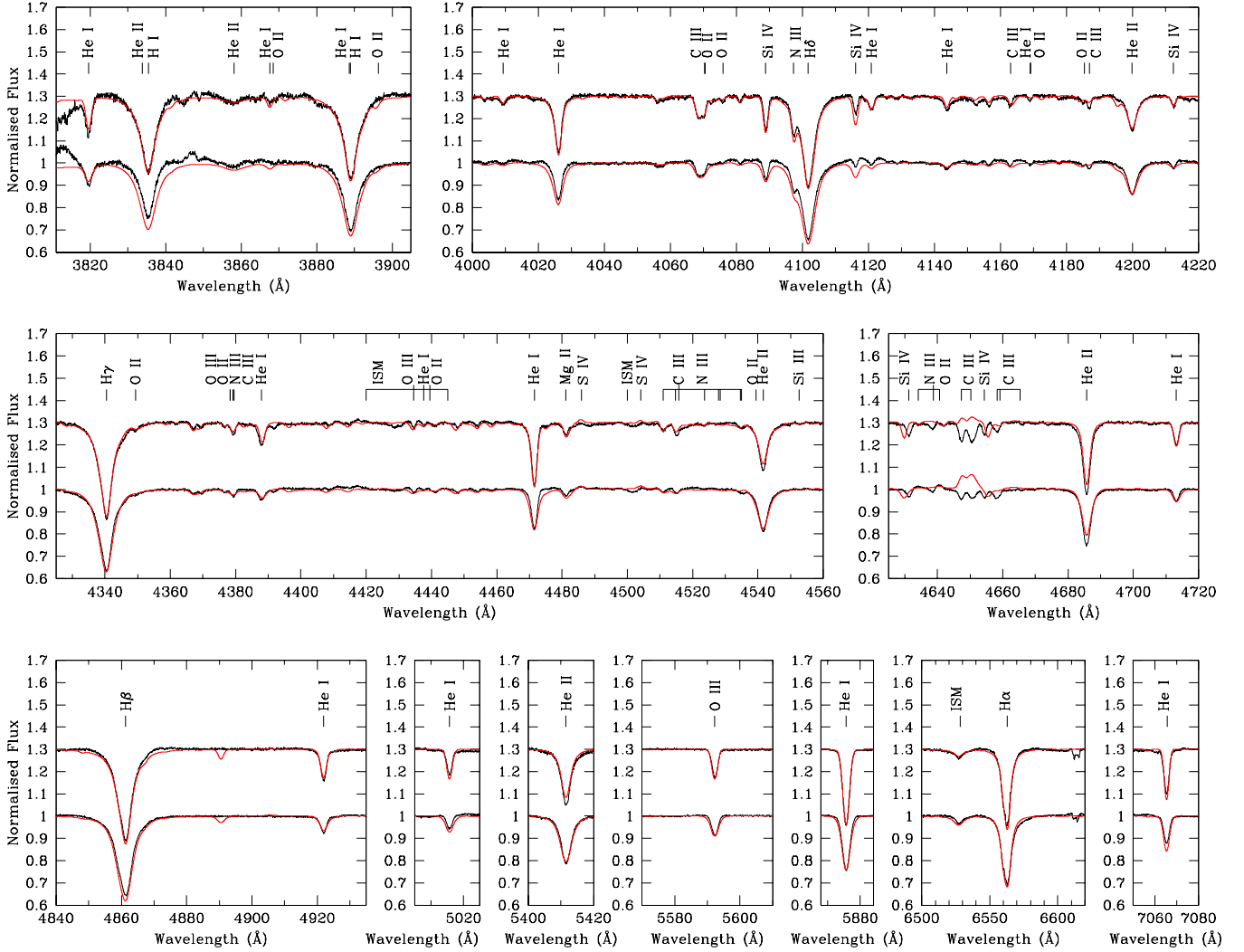
Figure 3. Normalised disentangled spectra (in black) of the primary and secondary stars of HD 165052 (the spectrum of the secondary star is shifted by +0.3 in the *y*-axis for clarity) together with the respective best-fit CMFGEN model atmosphere (in red).

4 RADIAL VELOCITY ANALYSIS

Our total set of RV measurements consists of our 71 primary and secondary RVs determined as part of the disentangling process (see Sect. 3.1) complemented by 94 primary and secondary RVs coming from the literature. Twelve RVs come from Morrison & Conti (1978) but we adopted the corrected values by Stickland et al. (1997). The latter authors do not report uncertainties on their measurements, and we therefore assumed symmetric uncertainties of 15 km s^{-1}, as representative of the O-C. Fifteen RVs come from Stickland et al. (1997), and we assumed symmetric uncertainties on these RVs of 10 km s^{-1} as representative of the O-C. Thirty RVs come from Arias et al. (2002) and (J. I. Arias, private communication, 2021), for which we adopted the uncertainties quoted by the authors. The remaining 37 RVs come from Ferrero et al. (2013) that we recalculated here (see Appendix B). We ended up, in total, with a series of 165 RVs spanning about 46 years. For the RVs derived from the spectral disentangling, we adopted formal errors of 3 km s^{-1}, as the small errors derived as part of the disentangling method would bias the adjustment given our high number of RVs compared to those coming from

the literature. We then processed in the adjustment of the RVs along three different avenues.

First, for each time of observation *t*, we adjusted the primary RV data with the following relation

$$\mathrm{RV_P}(t) = \gamma_\mathrm{P} + K_\mathrm{P}[\cos(\phi(t) + \omega(t)) + e \cos \omega(t)], \quad (2)$$

where γ_P, K_P, e, and ω are the primary apparent systemic velocity, the semi-amplitude of the primary RV curve, the eccentricity, and the argument of periastron of the primary orbit, respectively. The true anomaly ϕ is inferred from the eccentric anomaly, itself computed through Kepler's equation, which involves both e and the anomalistic orbital period P_orb of the system. We accounted for the apsidal motion through the variation of ω with time following the relation

$$\omega(t) = \omega_0 + \dot{\omega}(t - T_0), \quad (3)$$

where $\dot{\omega}$ is the apsidal motion rate and ω_0 is the value of ω at the time of periastron passage T_0. Given that different spectral lines give potentially slightly different values of the apparent systemic velocities, and given that the different RVs were obtained based on different sets of lines, the systemic velocity of each subset of our
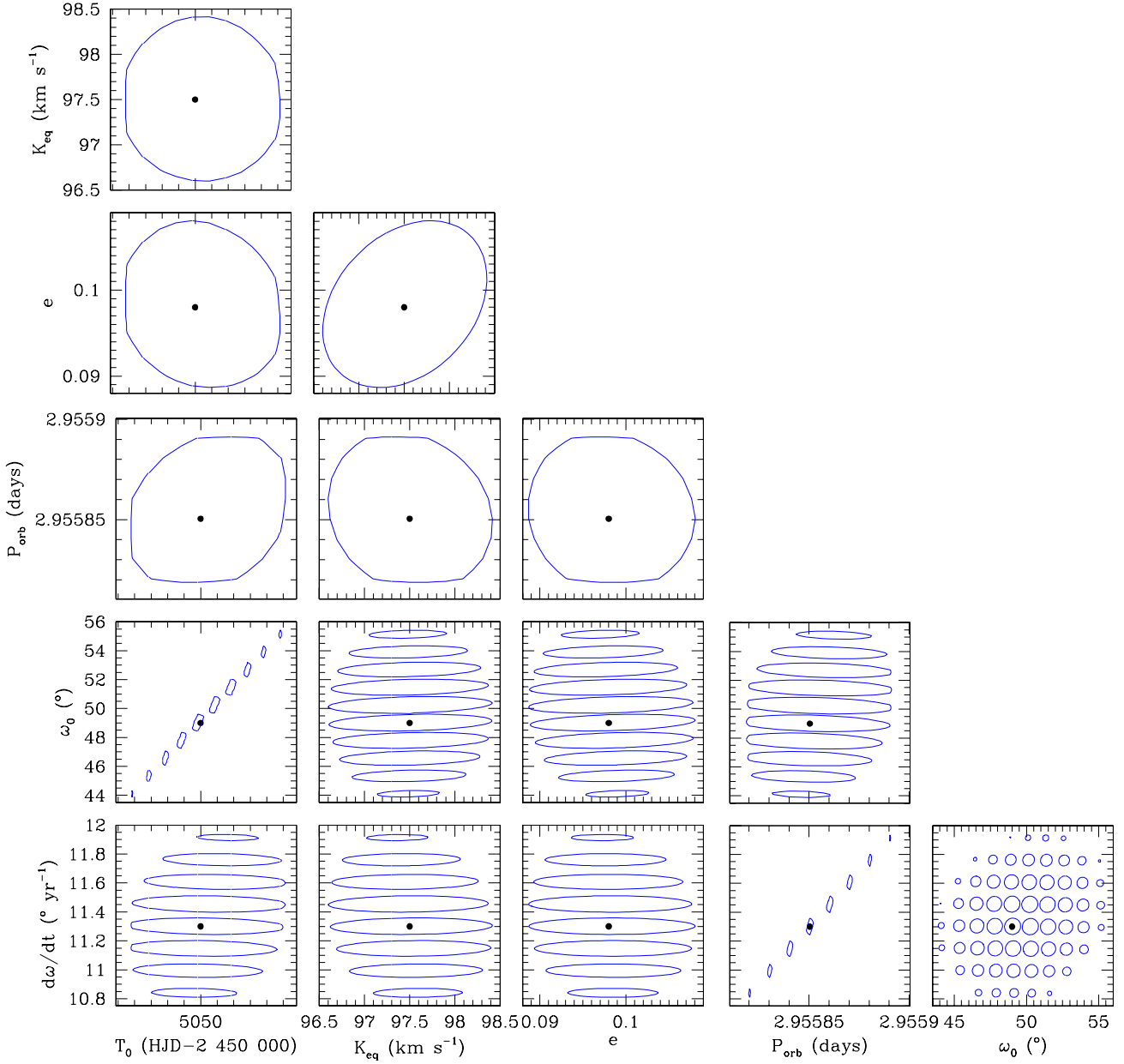
Figure 4. Confidence contours for the best-fit parameters obtained from the adjustment of the equivalent RV data of HD 165052. The best-fit solution is shown in each panel by the black filled dot. The corresponding 1σ confidence level is shown by the blue contour. We note the "zebra-like" strips for ω_0 and $\dot{\omega}$ are computational artefacts.

total dataset was adjusted so as to minimise the sum of the residuals of the data about the curve given by Eq. (2).

Second, we adjusted the secondary RV data with a relation similar to Eq. (2) corresponding to the secondary star, with K_S and γ_S having straightforward definitions.

Third, we made use of the linear relation

$$RV_P(t) = -qRV_S(t) + B \qquad (4)$$

relating the primary and secondary RVs of an SB2 system, where $q = \frac{M_S}{M_P}$ is the mass ratio and $B = \gamma_P + q\gamma_S$, to convert the RVs of both stars into equivalent RVs of the primary star with

$$RV_{eq}(t) = \frac{RV_P - qRV_S + B}{2}. \qquad (5)$$

to which we associate corresponding K_{eq} and γ_{eq}. We derived a value

$q = 0.902 \pm 0.009$ from the RVs coming from the disentangling process.

In the three cases, we scanned the 6-D parameter space in a systematic way to find the values of the free parameters (P_{orb}, e, T_0, ω_0, $\dot{\omega}$, and K_P or K_S or K_{eq}) that provide the best fit to the whole set of corresponding RV data. The projections of the 6-D parameter space onto the 2-D planes is illustrated in Fig. 4 for the equivalent RVs. The corresponding orbital parameters are given in Table 4. $a_P \sin i$ and $a_S \sin i$ stand for the minimum semi-major axis of the primary and secondary stars, respectively, $M_P \sin^3 i$ and $M_S \sin^3 i$ stand for the minimum mass of the primary and secondary stars, respectively, and χ^2_ν is the reduced χ^2. We note that in the case of the primary (respectively secondary) RVs, we used the mass ratio derived previously to convert K_P (respectively K_S) into a value for K_S (respectively K_P)
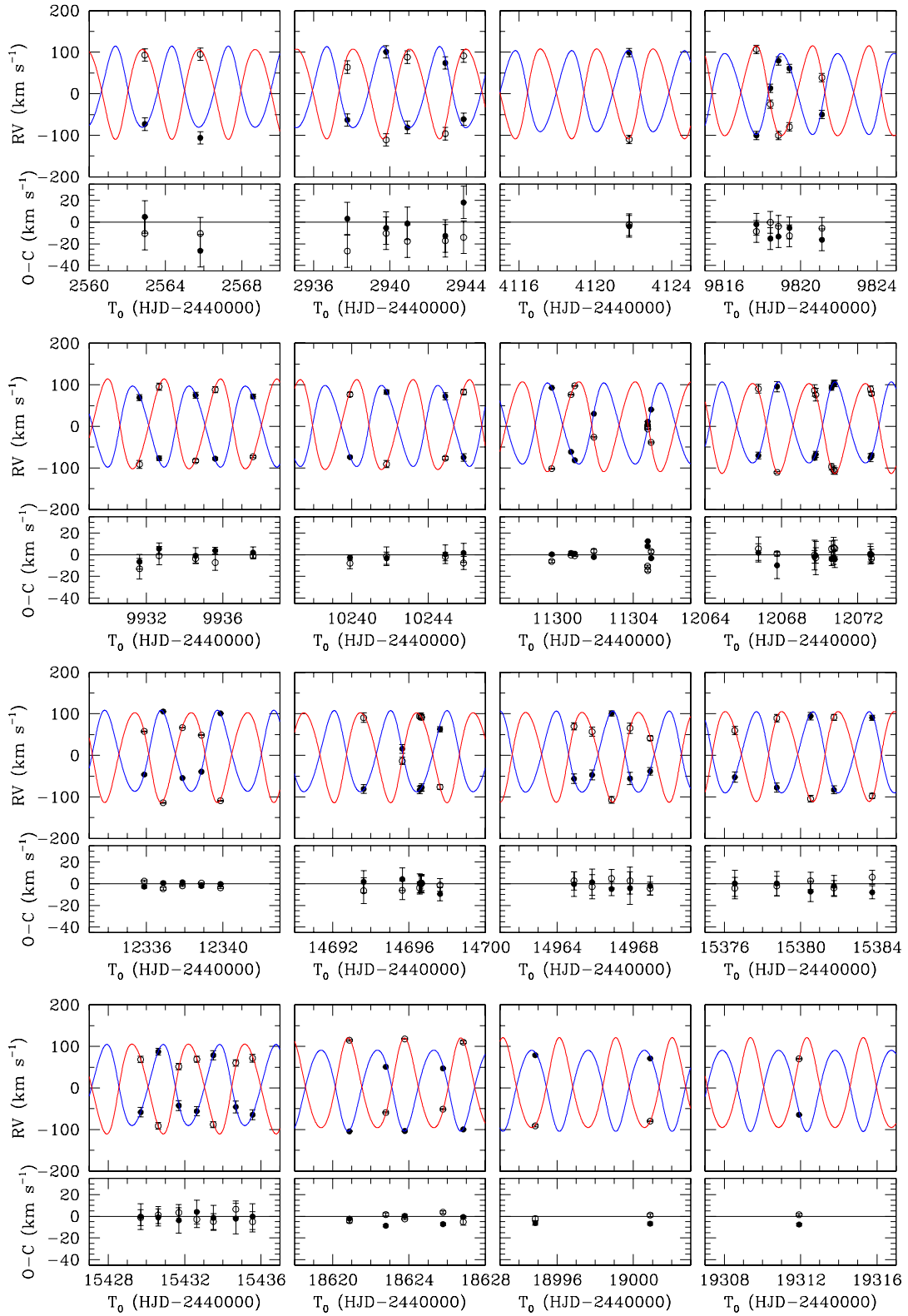
Figure 5. Comparison between the measured RVs of the primary (filled dots) and secondary (open dots) of HD 165052 with the orbital solution from the equivalent RVs (see last column in Table 4). The blue and red lines represent the fitted RV curve of the primary and secondary stars, respectively. The top panels correspond to data from Morrison & Conti (1978, *two left ones*) and Stickland et al. (1997, *two right ones*). The panels on the second row correspond to data from Arias et al. (2002, *the first, second, and fourth ones*) and to RVs derived in this paper (*third one*). The panels on the third row correspond to RVs derived in this paper (*first one*) and data from Ferrero et al. (2013, *last three ones*). The last row corresponds to data from Ferrero et al. (2013, *first one*) and to RVs derived in this work (*last three ones*).

Table 4. Best-fit orbital parameters of HD 165052 obtained from the adjustment of the RV data.

Parameter	Primary RVs	Secondary RVs	Equivalent RVs
e	$0.093^{+0.009}_{-0.008}$	0.096 ± 0.007	0.098 ± 0.010
$\dot{\omega}$ ($^\circ$ yr^{-1})	$12.02^{+0.63}_{-0.48}$	$10.72^{+0.50}_{-0.34}$	$11.30^{+0.64}_{-0.49}$
$P_{\rm orb}$ (d)	$2.95590^{+0.00004}_{-0.00003}$	2.95581 ± 0.00003	$2.95585^{+0.00004}_{-0.00003}$
ω_0 ($^\circ$)	$52.8^{+5.2}_{-6.3}$	$50.1^{+3.9}_{-5.1}$	$49.0^{+6.4}_{-5.2}$
T_0 (HJD)	$2\,455\,050.03^{+0.04}_{-0.05}$	$2\,455\,050.01^{+0.04}_{-0.05}$	$2\,455\,050.00^{+0.05}_{-0.04}$
$K_{\rm P}$ (km s^{-1})	97.3 ± 0.8	96.8 ± 1.2	97.5 ± 0.9
$K_{\rm S}$ (km s^{-1})	107.9 ± 1.4	$107.4^{+0.7}_{-0.8}$	108.1 ± 1.5
$K_{\rm eq}$ (km s^{-1})	...	...	97.5 ± 0.9
$q = M_{\rm S}/M_{\rm P}$	0.902 ± 0.009	0.902 ± 0.009	0.902 ± 0.009
$a_{\rm P}\ \sin i$ ($R_\odot$)	5.66 ± 0.04	5.63 ± 0.05	5.66 ± 0.05
$a_{\rm S}\ \sin i$ ($R_\odot$)	6.27 ± 0.06	$6.24^{+0.04}_{-0.05}$	6.28 ± 0.06
$M_{\rm P}\ \sin^3 i$ ($M_\odot$)	1.37 ± 0.04	1.35 ± 0.04	1.38 ± 0.05
$M_{\rm S}\ \sin^3 i$ ($M_\odot$)	1.24 ± 0.04	$1.22^{+0.03}_{-0.04}$	1.24 ± 0.04
χ^2_ν	1.465	2.155	0.971

In the case of the primary (respectively secondary) RVs, we used the mass ratio derived in Sect. 4 to convert $K_{\rm P}$ (respectively $K_{\rm S}$) into a value for $K_{\rm S}$ (respectively $K_{\rm P}$) and compute the minimum masses but we did not adjust the secondary (respectively primary) RVs directly.

and compute the associated minimum masses but we did not adjust the secondary (respectively primary) RVs directly. Figure 5 illustrates the best fit of the RV data with the equivalent RVs solution at 16 different epochs.

The eccentricities we obtained for the three solutions are compatible, within the error bars, with those coming from the literature (see Table 1), except with the value of Stickland et al. (1997) as these authors explicitly assumed a zero eccentricity for the system. Our orbital periods are longer and not compatible, within the error bars, with those coming from the literature (we did not consider the one of Morrison & Conti (1978), see discussion in Sect. 1). Our value of $K_{\rm P}$ is compatible, within the error bars, with those of Stickland et al. (1997), Linder et al. (2007), and Ferrero et al. (2013), but slightly larger than the one quoted by Arias et al. (2002). Our value of $K_{\rm S}$ is compatible with those of Stickland et al. (1997), and Ferrero et al. (2013) but slightly larger than the one quoted by Arias et al. (2002) and slightly smaller than the one quoted by Linder et al. (2007, see Table 1). Our mass ratio is compatible, within the error bars, with those coming from the literature, except for the one quoted by Linder et al. (2007, see Table 1). Finally, our apsidal motion rates are slightly smaller than the value of $(12.1 \pm 0.3)^\circ$ yr^{-1} reported by Ferrero et al. (2013) but, in the cases of the primary and equivalent RVs solutions, still in agreement within the error bars.

5 STELLAR STRUCTURE AND EVOLUTION TRACKS

We computed stellar structure and evolution tracks with the Code Liégeois d'Évolution Stellaire[1] (Clés, Scuflaire et al. 2008, see also Rosu et al. (2020a) for the main features of Clés used in the present context). The first goal of this theoretical analysis is to derive evolutionary masses for the stars and, hence, to put a constraint on the value of the inclination of the orbit through the confrontation with the minimum stellar masses derived in Sect. 4. The second goal of this analysis is to see how the theoretical apsidal motion rates derived for two stellar models of the same age compare to the observational apsi-

[1] The Clés code is developed and maintained by Richard Scuflaire at the STAR Institute at the University of Liège.

dal motion rate. In the present analysis, we assumed that HD 165052 has an age of 2.0 ± 0.5 Myr (see Sect. 1).

The apsidal motion rate of a binary system, in the simple two-body case, is the sum of a Newtonian contribution (N) and a general relativistic correction (GR), which expressions were introduced by Sterne (1939) for the former one, and Shakura (1985) and Giménez (1985) for the latter one. We here adopt the same conventions and notations as in Rosu et al. (2020a) (see Sects. 3 and 4, and Equations (17) to (20) and (5) to (9)).

We built a grid of stellar evolution tracks having an initial mass $M_{\rm init}$ ranging from 18 to 27 $M_\odot$ and a turbulent diffusion coefficient D_T of 0, 10^7, 2×10^7, and 3×10^7 cm^2 s^{-1}, and for which we adopted a standard mass-loss scaling factor $\xi = 1$ and an overshooting parameter $\alpha_{\rm ov} = 0.30$ (see Rosu et al. 2020a, 2022a,b, for a description of these parameters and a discussion of their impact and their standard values). We present in the Hertzsprung-Russell diagrams in Figs. 6 and 7 the evolutionary tracks for the primary and secondary stars, respectively. For better visibility in the diagrams, we decided to only present the tracks that cross the observational boxes defined by the observational effective temperatures and bolometric luminosities of the stars. Among these selected models, we discarded those having an age lower than 1.5 Myr or higher than 2.5 Myr when crossing the observational box in the Hertzsprung-Russel diagram. Given the conclusions reached by Rosu et al. (2020a, 2022a,b) about the necessity to include enhanced turbulent mixing in the stellar evolution models to reproduce the internal structure of the massive stars they studied, it is highly unlikely that a model without any turbulent diffusion would be representative of the stars of HD 165052. Hence, we further discarded the tracks having $D_T = 0$ cm^2 s^{-1}. We were thus left with nine tracks for the primary star and seven tracks for the secondary star.

For each selected evolutionary track, we report in Table 5 the evolutionary mass, radius, effective temperature, and internal stellar structure constant corrected for the effects of rotation following Claret (1999) at the ages of 1.5, 2.0, and 2.5 Myr. The comparison between models of same initial mass and same current age shows us that the turbulent diffusion coefficient has a negligible impact on the current mass of the model and has only a small impact on the current radius and internal stellar structure constant of the model. This behaviour is not surprising given that the star is very young and, hence, the
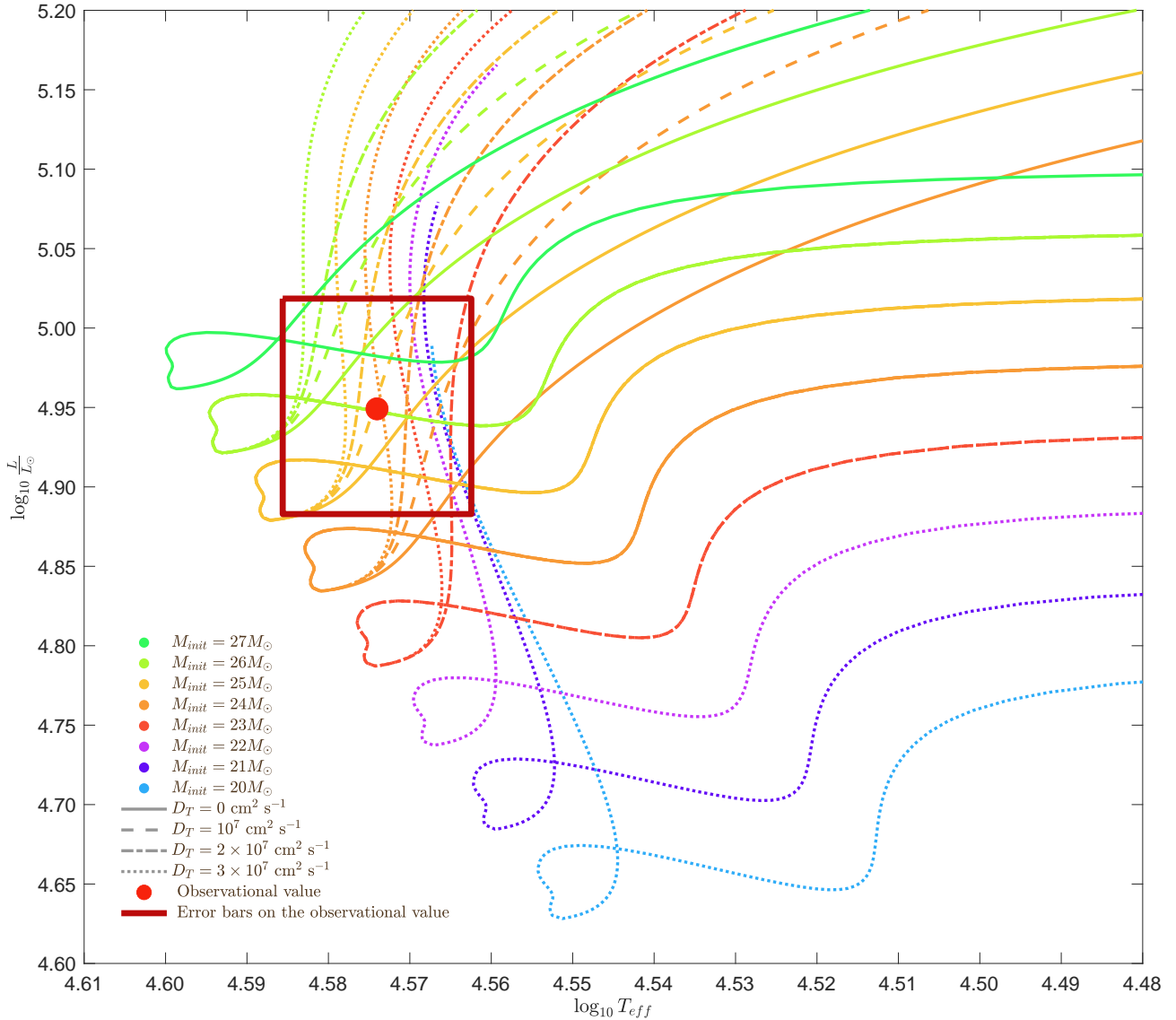
Figure 6. Hertzsprung-Russell diagram: evolutionary tracks of `Clés` models for the primary star of M_{init} = 20 $M_{\odot}$ (light blue), 21 $M_{\odot}$ (purple), 22 $M_{\odot}$ (plum), 23 $M_{\odot}$ (coral), 24 $M_{\odot}$ (orange), 25 $M_{\odot}$ (yellow), 26 $M_{\odot}$ (lime), and 27 $M_{\odot}$ (watergreen), and D_T = 0 cm^2 s^{-1} (solid line), 10^7 cm^2 s^{-1} (dashed line), 2 $\times$ 10^7 cm^2 s^{-1} (dotted-dashed line), and 3 $\times$ 10^7 cm^2 s^{-1} (dotted line). All models have ξ = 1 and α_{ov} = 0.30. The observational value is represented by the red point, and its error bars are represented by the dark red rectangle.

turbulent mixing occurring in its interior did not act for a long enough time to produce important changes to both the radius and the internal stellar structure constant.

Assuming that the primary model with M_{init} = 25 $M_{\odot}$ and D_T = 2 $\times$ 10^7 cm^2 s^{-1} and the secondary model with M_{init} = 21 $M_{\odot}$ and D_T = 2 $\times$ 10^7 cm^2 s^{-1}, both at ages 2 Myr, are representative of the stars, we infer evolutionary masses $M_{ev,P}$ = 24.8 $\pm$ 1.0 $M_{\odot}$ and $M_{ev,S}$ = 20.9 $\pm$ 1.0 $M_{\odot}$, where the subscript P and S stand for the primary and secondary stars, respectively, evolutionary radii $R_{ev,P}$ = $7.0^{+0.5}_{-0.4}$ $R_{\odot}$ and $R_{ev,S}$ = $6.2^{+0.4}_{-0.3}$ $R_{\odot}$, and internal stellar structure constants corrected for the stellar rotation following Claret (1999) $k_{2,P}$ = $1.20^{+0.13}_{-0.16}$ $\times$ 10^{-2} and $k_{2,S}$ = $1.26^{+0.09}_{-0.12}$ $\times$ 10^{-2}, where the angular rotation velocities Ω were computed using the projected rotational velocities derived in Sect. 3.3 corrected for the inclination. The error bars include the differences coming from a difference of 1.0 $M_{\odot}$ in M_{init}, of 1$\times$10^7 cm^2 s^{-1} in D_T, and of 0.5 Myr in the stellar

age. The evolutionary mass ratio of the binary amounts to $0.84^{+0.08}_{-0.07}$, slightly smaller than but still within the error bars of the observational mass ratio. Combined with the minimum masses obtained in Sect. 4 (see last column of Table 4), the evolutionary masses put a constraint on the orbital inclination: 22.1° $\leq$ i $\leq$ 23.3°. This small value of the inclination indicates that eclipses are very unlikely to be seen in photometric observations of this binary system (see also Fig. 8).

We then computed theoretical values for the apsidal motion rate. We adopted models for the primary and secondary stars of the same age and combined all the possible pairs given in Table 5. The semi-major axis is computed through the Kepler's third law for the corresponding combination of primary and secondary masses whilst the rotational periods of the stars are computed using the projected rotational velocities derived in Sect. 3.3 corrected for the inclination. The results are provided in Table 6: We adopted the models having an age of 2.0 Myr as our reference models and computed the error bars
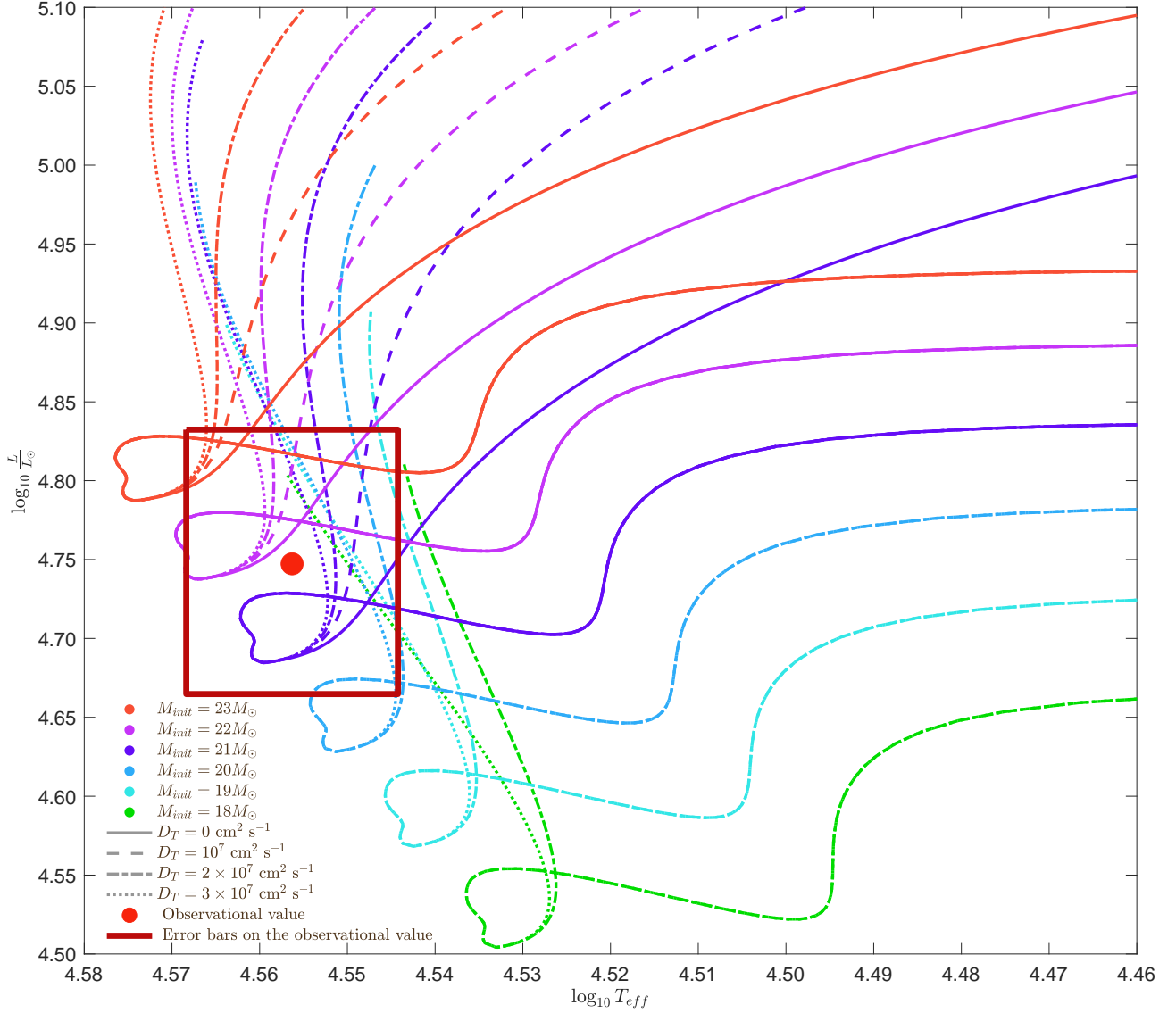
Figure 7. Hertzsprung-Russell diagram: evolutionary tracks of `Clés` models for the secondary star of $M_{\rm init} = 18\,M_\odot$ (green), $19\,M_\odot$ (turquoise), $20\,M_\odot$ (light blue), $21\,M_\odot$ (purple), $22\,M_\odot$ (plum), and $23\,M_\odot$ (coral), and $D_T = 0\,{\rm cm^2\,s^{-1}}$ (solid line), $10^7\,{\rm cm^2\,s^{-1}}$ (dashed line), $2 \times 10^7\,{\rm cm^2\,s^{-1}}$ (dotted-dashed line), and $3 \times 10^7\,{\rm cm^2\,s^{-1}}$ (dotted line). All models have $\xi = 1$ and $\alpha_{\rm ov} = 0.30$. The observational value is represented by the red point, and its error bars are represented by the dark red rectangle.

based on models of 1.5 and 2.5 Myr. All theoretical apsidal motion rates agree with the observational determination (see last column in Table 4) except those computed combining the pairs of models PM24DT2-SM20DT3 and PM24DT3-SM20DT3 that slightly underestimate the apsidal motion rate compared to the observational value. This confrontation between observational and theoretical apsidal motion rates allows us to confirm the inferred evolutionary masses and radii of the stars.

Finally, we computed the observational weighted-average mean of the internal structure constants of the stars, $k_{2,{\rm obs}}$, as defined by Equations (18) and (19) in Rosu et al. (2022a), adopting an inclination of $22.7° \pm 0.6°$ while all other parameters are taken from observational determinations. We obtained $k_{2,{\rm obs}} = 1.36^{+0.44}_{-0.43} \times 10^{-2}$, a value slightly larger but still compatible with the theoretical determinations for the two stars within the error bars.

6 CONCLUSION

We presented a new, in depth spectroscopic analysis of medium- and high-resolution spectra of the massive eccentric binary system HD 165052 and derived the first self-consistent orbital solution of all existing RV data, including those reported in the literature, accounting for the change of the longitude of periastron with time.

We applied our disentangling code based on the method of González & Levato (2006) to derive the RVs of the stars at each time of observations. Then, we applied the advanced disentangling method proposed by Quintero et al. (2020), that allows the reconstruction of artefact-free individual spectra, to the spectroscopic observations to reconstruct the spectra of the components. These latter were analysed, for the first time, with the non-LTE model atmosphere code `CMFGEN` to derive fundamental stellar and wind parameters.

We performed the RV analysis of all data, including those coming

Table 5. Properties of stellar structure and evolution models for the primary and secondary stars of HD 165052 at the ages of 1.5, 2.0, and 2.5 Myr. Column 1 gives the name of the model. Columns 2 and 3 give the initial mass M_{init} and the turbulent diffusion coefficient D_T of the evolutionary track. Columns 4, 7, and 10 give the current mass M of the model. Columns 5, 8, and 11 give the current radius R of the model. Columns 6, 9, and 12 give the internal stellar structure constant k_2 of the model corrected for the effects of rotation according to Claret (1999).

	Evolutionary track		Age = 1.5 Myr			Age = 2.0 Myr			Age = 2.5 Myr		
Name	M_{init} ($M_\odot$)	D_T (cm^2 s^{-1})	M ($M_\odot$)	R ($R_\odot$)	k_2 (10^{-2})	M ($M_\odot$)	R ($R_\odot$)	k_2 (10^{-2})	M ($M_\odot$)	R ($R_\odot$)	k_2 (10^{-2})
Primary star											
PM24DT1	24	1×10^7	23.86	6.68	1.30	23.81	6.87	1.20	23.75	7.07	1.09
PM24DT2	24	2×10^7	23.86	6.64	1.32	23.81	6.81	1.22	23.75	6.97	1.12
PM24DT3	24	3×10^7	23.86	6.61	1.33	23.81	6.76	1.23	23.75	6.90	1.15
PM25DT1	25	1×10^7	24.83	6.87	1.29	24.77	7.07	1.18	24.69	7.29	1.06
PM25DT2	25	2×10^7	24.83	6.83	1.31	24.77	7.00	1.20	24.69	7.19	1.09
PM25DT3	25	3×10^7	24.83	6.79	1.32	24.76	6.95	1.22	24.69	7.12	1.12
PM26DT1	26	1×10^7	25.80	7.05	1.28	25.72	7.27	1.16	25.63	7.52	1.04
PM26DT2	26	2×10^7	25.80	7.01	1.29	25.72	7.21	1.18	25.62	7.41	1.06
PM26DT3	26	3×10^7	25.80	6.97	1.31	25.72	7.15	1.19	25.62	7.33	1.09
Secondary star											
SM20DT3	20	3×10^7	19.95	5.86	1.35	19.93	5.96	1.29	19.90	6.05	1.23
SM21DT1	21	1×10^7	20.93	6.11	1.33	20.90	6.25	1.24	20.87	6.39	1.16
SM21DT2	21	2×10^7	20.93	6.08	1.34	20.90	6.20	1.26	20.87	6.32	1.19
SM21DT3	21	3×10^7	20.93	6.05	1.35	20.90	6.16	1.28	20.87	6.26	1.21
SM22DT1	22	1×10^7	21.91	6.31	1.32	21.88	6.46	1.23	21.84	6.62	1.14
SM22DT2	22	2×10^7	21.91	6.27	1.33	21.88	6.40	1.25	21.84	6.54	1.17
SM22DT3	22	3×10^7	21.91	6.24	1.34	21.88	6.36	1.27	21.84	6.48	1.19

Table 6. Theoretical values of the apsidal motion rate (in $^\circ$ yr^{-1}) in HD 165052. The values are obtained with models for the primary and secondary stars of 2.0 Myr and the error bars are computed using models of 1.5 and 2.5 Myr.

	SM20DT3	SM21DT1	SM21DT2	SM21DT3	SM22DT1	SM22DT2	SM22DT3
PM24DT1	$10.54^{+0.34}_{-0.36}$	$11.13^{+0.43}_{-0.45}$	$11.00^{+0.38}_{-0.40}$	$10.92^{+0.35}_{-0.38}$	$11.52^{+0.47}_{-0.46}$	$11.38^{+0.41}_{-0.41}$	$11.29^{+0.37}_{-0.39}$
PM24DT2	$10.41^{+0.28}_{-0.31}$	$10.99^{+0.37}_{-0.40}$	$10.87^{+0.32}_{-0.36}$	$10.78^{+0.29}_{-0.33}$	$11.39^{+0.41}_{-0.41}$	$11.25^{+0.34}_{-0.37}$	$11.15^{+0.31}_{-0.34}$
PM24DT3	$10.32^{+0.25}_{-0.28}$	$10.90^{+0.34}_{-0.37}$	$10.78^{+0.28}_{-0.33}$	$10.69^{+0.26}_{-0.30}$	$11.30^{+0.37}_{-0.38}$	$11.15^{+0.31}_{-0.34}$	$11.06^{+0.28}_{-0.31}$
PM25DT1	$10.85^{+0.38}_{-0.38}$	$11.44^{+0.46}_{-0.47}$	$11.31^{+0.41}_{-0.42}$	$11.22^{+0.38}_{-0.40}$	$11.83^{+0.50}_{-0.48}$	$11.69^{+0.44}_{-0.43}$	$11.59^{+0.41}_{-0.41}$
PM25DT2	$10.71^{+0.31}_{-0.32}$	$11.29^{+0.39}_{-0.41}$	$11.16^{+0.34}_{-0.37}$	$11.08^{+0.31}_{-0.35}$	$11.68^{+0.43}_{-0.43}$	$11.54^{+0.37}_{-0.38}$	$11.45^{+0.34}_{-0.35}$
PM25DT3	$10.61^{+0.26}_{-0.29}$	$11.20^{+0.35}_{-0.38}$	$11.07^{+0.30}_{-0.34}$	$10.98^{+0.27}_{-0.32}$	$11.59^{+0.38}_{-0.40}$	$11.45^{+0.32}_{-0.35}$	$11.35^{+0.29}_{-0.32}$
PM26DT1	$11.18^{+0.40}_{-0.40}$	$11.76^{+0.49}_{-0.49}$	$11.63^{+0.44}_{-0.45}$	$11.54^{+0.41}_{-0.42}$	$12.14^{+0.52}_{-0.50}$	$12.00^{+0.46}_{-0.46}$	$11.91^{+0.43}_{-0.43}$
PM26DT2	$11.02^{+0.33}_{-0.35}$	$11.60^{+0.41}_{-0.44}$	$11.47^{+0.36}_{-0.39}$	$11.39^{+0.33}_{-0.37}$	$11.99^{+0.45}_{-0.45}$	$11.84^{+0.39}_{-0.40}$	$11.75^{+0.35}_{-0.37}$
PM26DT3	$10.91^{+0.28}_{-0.31}$	$11.49^{+0.37}_{-0.40}$	$11.36^{+0.32}_{-0.35}$	$11.28^{+0.29}_{-0.33}$	$11.88^{+0.40}_{-0.41}$	$11.74^{+0.34}_{-0.36}$	$11.64^{+0.31}_{-0.34}$

from the literature, along three avenues: considering the primary RVs only, the secondary RVs only, and converting the primary and secondary RVs into primary-equivalent RVs. In all three cases, we obtained orbital solutions which were in agreement within their error bars. We adopted the equivalent RVs solution as the final solution and hence, concluded that the apsidal motion rate in the system amounts to $(11.30^{+0.64}_{-0.49})^\circ$ yr^{-1}. We conclude that our analysis of the spectroscopic observations of HD 165052 and the analysis of the RVs of the stars explicitly accounting for the apsidal motion allow us to derive a consistent measure of the apsidal motion rate in the binary. Our analysis of all available RV data also allowed us to determine more reliably the orbital parameters of the binary. Our values differ from those of Stickland et al. (1997), Arias et al. (2002), and Linder et al. (2007) mainly because we explicitly accounted for the apsidal motion in the RV analysis. Our results differ from those of Ferrero et al. (2013) mainly due to the increased number of RV data available at the time of our study.

We computed dedicated stellar structure and evolution tracks with Clés assuming the stellar effective temperatures and luminosities obtained as part of the CMFGEN analysis, and an age of 2.0 ± 0.5 Myr for

the binary. We derived evolutionary masses $M_{\mathrm{ev,P}} = 24.8 \pm 1.0\ M_\odot$ and $M_{\mathrm{ev,S}} = 20.9 \pm 1.0\ M_\odot$ and evolutionary radii $R_{\mathrm{ev,P}} = 7.0^{+0.5}_{-0.4}\ R_\odot$ and $R_{\mathrm{ev,S}} = 6.2^{+0.4}_{-0.3}\ R_\odot$ for the primary and secondary stars, respectively. Through the confrontation with the minimum stellar masses, we constrained the orbital inclination: $22.1^\circ \le i \le 23.3^\circ$. We computed theoretical apsidal motion rates adopting two stellar models of the same age and observed that these were in agreement with the observational apsidal motion rate, therefore enforcing the inferred values of the evolutionary stellar masses and radii, and putting some constraints on the density stratification inside the stars through the internal stellar structure constants.

Whilst our results exclude the possibility of photometric eclipses, it would nevertheless be worth to acquire high-precision space-borne photometry to look for low-level photometric variability due to a phase-dependent tidal distortion of the stars and/or tidally-induced pulsations (e.g., Kołaczek-Szymański et al. 2021). Adopting our best estimates of the stellar parameters, we used the Nightfall code to simulate synthetic lightcurves of HD 165052 for different values of the orbital inclination between 17.5° and 27.5° (see Fig. 8). In all cases, we found that the lightcurve is dominated by the so-called
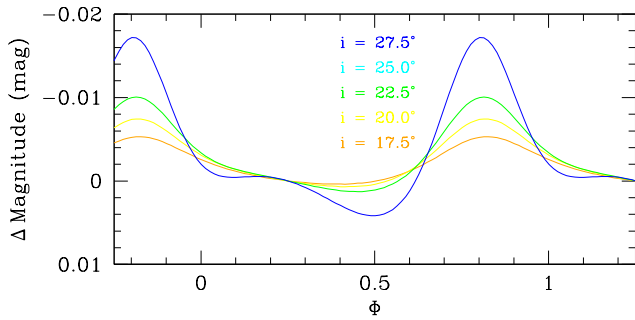
Figure 8. Synthetic lightcurves of HD 165052 for different values of the orbital inclination between 17.5° and 27.5°. We note that the exact shape of the lightcurves depends on the ω-value, hence on the assumed observational date; in the present case we fixed the date to HJD 2 460 000.

heartbeat variations due to the orbital eccentricity rather than by ellipsoidal variations. For the most likely inclination near 22.5°, we expect peak-to-peak amplitudes of about 0.01 mag which are certainly within reach of sensitive space-borne photometry. We inspected both ASAS and Hipparcos photometric data. No significative variation is observed for the ASAS lightcurve and the error bars on the data are larger than the expected variations. Whilst the Hipparcos data have lower error bars than the ASAS data, the errors remain quite large and the data do not sample the most interesting parts of the orbit, namely the phases close to periastron passage. Unfortunately, there exist currently no other high-precision space-borne photometric data. Hence, the existing data cannot be used to study the light curve of this system. Whereas heartbeat variations could help confirming the estimate of the orbital inclination that we have obtained, the detection of pulsations would offer the possibility to gain further insight into the internal structure of the stars that would offer a powerful tool for comparison with the `Clés` models that we have tested here.

DATA AVAILABILITY

The ESO and CFHT data used in this study are available from the corresponding archives, whilst the TIGRE spectra can be made available upon reasonable request.

REFERENCES

Arias, J. I., Morrell, N. I., Barbá, R. H., et al. 2002, MNRAS, 333, 202
Asplund, M., Grevesse, N., Sauval, A. J., & Scott, P. 2009, ARA&A, 47, 481
Bailer-Jones, C. A. L., Rybizki, J., Fouesneau, M., Demleitner, G., & Andrae, R. 2021, AJ, 161, 147
Böhm-Vitense, E., Hodge, P., & Boggs, D. 1984, ApJ, 287, 825
Brott, I., de Mink, S. E., Cantiello, M., et al. 2011, A&A, 530, A115
Claret, A. 1999, A&A, 350, 56
Claret, A., & Giménez, A. 2010, A&A, 519, A57
Claret, A., Giménez, A., Baroch, A., et al. 2021, A&A, 654, A17
Claret, A., & Torres, G. 2019, ApJ, 876, 134
Conti, P. S. 1974, ApJ, 187, 539
Conti, P. S., & Alschuler, W. R. 1971, ApJ, 170, 325
Conti, P. S., & Ebbets, D. 1977, ApJ, 213, 438
Damiani, F., Flaccomio, E., Micela, et al. 2004, ApJ, 608, 781
Dekker, H., D'Odorico, S., Kaufer, A., Delabre, B., & Kotzlowski, H. 2000, Proceedings SPIE, 4008, 534
Donati, J.-F. 2003, ASP Conference Series, 307, 41
Duchêne, G., & Kraus, A. 2013, ARA&A, 51, 269
Ekström, S., Georgy, C., Eggenberger, P., et al. 2012, A&A, 537, A146
Ferrero, G., Gamen, R., Benvenuto, O., & Fernández-Lajús, E. 2013, MNRAS, 433, 1300
Gaia Collaboration, Brown, A. G. A., Vallenari, A., Prusti, T., et al. 2021, A&A, 649, A1
Giménez, A. 1985, ApJ, 297, 405
González, J. F., & Levato, H. 2006, A&A, 448, 283
González-Pérez, J. N., Mittag, M., Schmitt, J. H. M. M., et al. 2022, FrASS, 9, 912546
Gray, D. F. 2005, The Observation and Analysis of Stellar Photospheres (Cambridge University Press)
Gray, D. F. 2008, The Observation and Analysis of Stellar Photospheres, 3rd edn. (Cambridge University Press)
Hejlesen, P. M. 1987, A&AS, 69, 251
Hillier, D. J., & Miller, D. L. 1998, ApJ, 496, 407
Howarth, I. D., Siebert, K. W., Hussain, G. A. J., & Prinja, R. K. 1997, MNRAS, 284, 265
Kaufer, A., Stahl, O., Tubbesing, S., et al. 1999, The Messenger, 85, 8
Kilambi, G. C. 1977, MNRAS, 178, 423
Kołaczek-Szymański, P. A., Pigulski, A., Michalska, G., Moździerski, D., & Różański, T. 2021, A&A, 647, A12
Linder, N., Rauw, G., Sana, H., De Becker, M., & Gosset, E. 2007, A&A, 474, 193
Marchenko, S. V., Moffat, A. F. J., & Eenens, P. 1998, PASP, 110, 1416
Martins, F. 2011, Bulletin de la Société Royale des Sciences de Liège, 80, 29
Martins, F., & Hillier, D. J. 2012, A&A, 545, A95
Martins, F., & Plez, B. 2006, A&A, 457, 637
Martins, F., Schaerer, D., & Hillier, D. J. 2005, A&A, 436, 1049
Mathys, G. 1988, A&AS, 76, 427
Mayne, N. J., & Naylor, T. 2008, MNRAS, 386, 261
Mazeh, T. 2008, EAS Publications Series, 29, 1
Morrison, N. D., & Conti, P. S. 1978, AJ, 224, 558
Muijres, L. E., Vink, J. S., de Koter, A., Müller, P. E., & Langer, N. 2012, A&A, 537, A37
Palate, M., & Rauw, G. 2012, A&A, 537, A119
Plaskett, J. S. 1924, PDAO, 2, 287
Penny, L. R. 1996, PhD thesis, Georgia State University
Prisinzano, L., Damiani, F., Micela, G., & Sciortino, S. 2005, A&A, 430, 941
Quintero, E. A., Eenens, P., & Rauw, G. 2020, Astronomische Nachrichten, 341, 628
Rosu, S., Noels, A., Dupret, M.-A., et al. 2020a, A&A, 642, A221
Rosu, S., Rauw, G., Conroy, K. E., et al. 2020b, A&A, 635, A145
Rosu, S., Rauw, G., Farnir, M., Dupret, M.-A., & Noels, A. 2022a, A&A, 660, A120
Rosu, S., Rauw, G., Nazé, Y., Gosset, E., & Sterken, C. 2022b, A&A, 664, A98
Sagar, R., & Joshi, U. C. 1978, MNRAS, 184, 467
Sana, H., de Mink, S. E., de Koter, A., et al. 2012, Science, 337, 444
Sana, H., Hensberge, H., Rauw, G., & Gosset, E. 2003, A&A, 405, 1063
Scuflaire, R., Théado, S., Montalbán, J., et al. 2008, Ap&SS, 316, 83
Shakura, N. I. 1985, Sov. Astron. Lett., 11, 224
Simón-Díaz, S., & Herrero, A. 2007, A&A, 468, 1063
Sterne, T. E. 1939, MNRAS, 99, 451
Stickland, D. J., Lloyd, C., & Koch, R. H. 1997, The Observatory, 117, 295
Sung, H., Chun, M., Bessell, M. 2000, AJ, 120, 333
Topasna, G. A., Jones, R. H., & Kaltcheva, N. T. 2020, PASP, 132, 044301

van Altena, W. F., & Jones, B. F. 1972, A&A, 20, 425
Vernet, J., Dekker, H., D'Odorico, S., et al. 2011, A&A, 536, A105
Walborn, N. R. 1972, AJ, 77, 312
Walborn, N. R. 1973, AJ, 78, 1067
Walborn, N. R., & Fitzpatrick, E. L. 1990, PASP, 102, 379
Wellstein, S., Langer, N., & Braun, H. 2001, A&A, 369, 939
Zacharias, N., Finch, C. T., Girard, T. M., et al. 2013, AJ, 145, 44

APPENDIX A: SPECTRAL DISENTANGLING BASED ON THE METHOD DESCRIBED BY González & Levato (2006)

This appendix provides the journal of the spectroscopic observations of HD 165052 (Table A1) and a detailed description of the spectral disentangling performed to derive the RVs of the stars.

For the disentangling, we used synthetic TLUSTY spectra with $T_{\rm eff} = 35\,000$ K, $\log g = 4.0$, and $v \sin i_{\rm rot} = 70$ km s^{-1} as cross-correlation templates in the determination of the RVs.

We performed the disentangling on 15 separate wavelength domains: B1[3810:4150] Å, B2[4150:4250] Å, B3[4300:4570] Å, B4[4600:5040] Å, B5[4600:4980] Å, B6[4800:5040] Å, B7[5380:5610] Å, B8[5380:5840] Å, B9[5790:5840] Å, B10[5380:5450] Å, B11[5380:5750] Å, and B12[5560:5840] Å in the blue domain, and R1[5860:5885] Å, R2[6500:6700] Å, and R3[7000:7100] Å in the red domain. As a first step, we only considered the FEROS, ESPaDOns, and TIGRE spectra as these spectra have a better resolution than the UVES and XSHOOTER spectra. We processed the wavelength domains (B1, B2, B3, B4, B7, B8, B9, R1, R2, and R3) to reproduce the individual spectra and simultaneously estimate the RVs of the stars. The TIGRE spectra cover all above-mentioned domains except for B8, and three FEROS spectra (taken at 2 451 304.7434, 2 451 304.7507, and 2 451 304.9309 HJD) do not cover the B2 domain due to instrumental artefacts in that wavelength domain. We averaged the RVs from the individual wavelength domains using weights corresponding to the number of strong lines present in these domains (five lines for B1, one for B2, three for B3, two for B4, two for B7, three for B8, two for B9, one for R1, one for R2, and one for R3). The resulting RVs of both stars are reported in Table A1 together with their 1σ errors. We then performed the disentangling on the ten domains covered by the XSHOOTER and UVES spectra (B1, B2, B3, B5, B6, B10, B11, B12, R2, and R3) with the RVs of XSHOOTER and UVES observations free to vary, and the RVs of the FEROS, ESPaDOns, and TIGRE spectra fixed to their previously computed weighted averages. Two UVES observations (taken at 2 452 584.5002 and 2 452 584.5161 HJD) cover the B1, B2, B3, and B5 domains only, the other two UVES observations (taken at 2 452 584.5216 and 2 452 584.5234 HJD) cover the B6, B10, B11, and R2 domains only, four XSHOOTER observations (taken at 2 457 583.7901, 2 457 583.7916, 2 457 954.7756, and 2 457 954.7772 HJD) cover the B1, B2, B3, B5, B6, and B10 domains only, and the remaining five XSHOOTER observations (taken at 2 457 583.7902, 2 457 583.7916, 2 457 583.8401, 2 457 954.7757, and 2 457 954.7773 HJD) cover the B12, R2, and R3 domains only. We averaged the RVs from the individual wavelength domains using weights corresponding to the number of strong lines present in these domains (five lines for B1, one for B2, three for B3, two for B5, one for B6, one for B10, two for B11, two for B12, one for R2, and one for R3). The resulting RVs of both stars are reported in Table A1 together with their 1σ errors.

APPENDIX B: JOURNAL OF THE RVS OF HD 165052 COMING FROM Ferrero et al. (2013)

This appendix provides the journal of the RVs of HD 165052 from Ferrero et al. (2013). Given that the authors do not provide any error bar on their mean RVs, we computed both the mean RVs and standard deviation based on their individual measurements given in their Table B2, which we provide in Table B1.

This paper has been typeset from a TEX/LATEX file prepared by the author.

Table A1. Journal of the spectroscopic observations of HD 165052.

HJD $-2\,450\,000$	ϕ	RV_P (km s^{-1})	RV_S (km s^{-1})	Instrumentation
1299.7250	0.236	92.8 ± 1.1	-101.8 ± 1.2	ESO 1.5 m + FEROS
1300.7319	0.577	-61.3 ± 1.5	76.4 ± 0.7	ESO 1.5 m + FEROS
1300.9264	0.643	-81.5 ± 1.2	97.5 ± 0.7	ESO 1.5 m + FEROS
1301.9281	0.982	30.5 ± 0.6	-26.0 ± 1.7	ESO 1.5 m + FEROS
1304.7434	0.934	4.5 ± 0.7	0.2 ± 0.9	ESO 1.5 m + FEROS
1304.7507	0.937	11.5 ± 0.3	-6.5 ± 1.2	ESO 1.5 m + FEROS
1304.9309	0.998	40.3 ± 0.4	-38.4 ± 1.4	ESO 1.5 m + FEROS
1323.8361	0.393	24.9 ± 1.3	-23.8 ± 2.2	ESO 1.5 m + FEROS
1327.6014	0.667	-88.6 ± 1.1	101.5 ± 0.6	ESO 1.5 m + FEROS
1327.9127	0.773	-88.8 ± 1.0	99.4 ± 0.6	ESO 1.5 m + FEROS
1670.7102	0.745	-83.0 ± 0.9	99.2 ± 0.7	ESO 1.5 m + FEROS
1671.7197	0.087	103.3 ± 1.1	-108.4 ± 1.7	ESO 1.5 m + FEROS
1672.7016	0.419	-9.5 ± 1.2	16.4 ± 0.9	ESO 1.5 m + FEROS
2335.8879	0.783	-46.2 ± 1.5	57.7 ± 0.8	ESO 1.5 m + FEROS
2336.8791	0.118	105.5 ± 0.7	-113.9 ± 1.1	ESO 1.5 m + FEROS
2337.8880	0.460	-54.3 ± 1.0	66.8 ± 0.6	ESO 1.5 m + FEROS
2338.8808	0.795	-39.3 ± 1.2	48.8 ± 0.6	ESO 1.5 m + FEROS
2339.8848	0.135	101.1 ± 0.6	-109.2 ± 0.9	ESO 1.5 m + FEROS
2381.7324	0.293	5.6 ± 1.0	-2.4 ± 1.3	ESO 1.5 m + FEROS
2382.8570	0.673	-81.7 ± 0.8	96.7 ± 0.6	ESO 1.5 m + FEROS
2383.8577	0.012	95.5 ± 0.7	-101.6 ± 1.1	ESO 1.5 m + FEROS
2584.5002	0.891	54.1 ± 1.6	-10.0 ± 1.2	ESO VLT + UVES
2584.5161	0.897	49.7 ± 1.4	-7.0 ± 0.5	ESO VLT + UVES
2584.5216	0.899	55.8 ± 2.5	-10.1 ± 1.2	ESO VLT + UVES
2584.5234	0.899	55.7 ± 2.6	-11.4 ± 1.7	ESO VLT + UVES
3130.9089	0.748	-25.2 ± 1.2	31.9 ± 0.7	ESO 2.2 m + FEROS
3134.9113	0.102	93.6 ± 0.8	-101.0 ± 1.0	ESO 2.2 m + FEROS
4212.8381	0.778	48.3 ± 0.3	-48.7 ± 1.0	ESO 2.2 m + FEROS
5351.9169	0.142	-39.3 ± 1.2	49.3 ± 0.8	CFHT 3.6 m + ESPaDOns
5351.9169	0.142	-39.3 ± 1.2	49.4 ± 0.8	CFHT 3.6 m + ESPaDOns
5351.9302	0.147	-41.6 ± 1.2	52.2 ± 0.8	CFHT 3.6 m + ESPaDOns
5351.9302	0.147	-41.7 ± 1.3	52.2 ± 0.8	CFHT 3.6 m + ESPaDOns
5351.9368	0.149	-43.4 ± 1.2	53.1 ± 0.8	CFHT 3.6 m + ESPaDOns
5351.9368	0.149	-43.4 ± 1.2	53.1 ± 0.8	CFHT 3.6 m + ESPaDOns
5351.9434	0.151	-44.4 ± 1.2	55.1 ± 0.8	CFHT 3.6 m + ESPaDOns
5351.9434	0.151	-44.3 ± 1.1	55.1 ± 0.8	CFHT 3.6 m + ESPaDOns
5351.9567	0.156	-47.0 ± 1.1	57.9 ± 0.9	CFHT 3.6 m + ESPaDOns
5351.9568	0.156	-46.9 ± 1.1	57.9 ± 0.9	CFHT 3.6 m + ESPaDOns
7583.7901	0.212	-83.2 ± 0.6	107.8 ± 0.7	ESO VLT + XSHOOTER
7583.7902	0.212	-77.3 ± 1.8	114.4 ± 1.9	ESO VLT + XSHOOTER
7583.7916	0.213	-83.2 ± 0.7	107.2 ± 0.7	ESO VLT + XSHOOTER
7583.7916	0.213	-74.3 ± 2.4	112.8 ± 1.5	ESO VLT + XSHOOTER
7583.8401	0.229	-73.8 ± 1.9	105.0 ± 2.5	ESO VLT + XSHOOTER
7954.7756	0.721	91.1 ± 0.7	-78.0 ± 0.8	ESO VLT + XSHOOTER
7954.7757	0.721	94.1 ± 2.5	-72.7 ± 2.2	ESO VLT + XSHOOTER
7954.7772	0.721	90.7 ± 0.7	-78.2 ± 0.9	ESO VLT + XSHOOTER
7954.7773	0.721	94.4 ± 2.9	-72.2 ± 2.3	ESO VLT + XSHOOTER
8574.9673	0.539	87.4 ± 1.2	-99.1 ± 0.8	TIGRE + HEROS
8577.9071	0.534	88.8 ± 1.2	-100.0 ± 1.0	TIGRE + HEROS
8577.9458	0.547	85.3 ± 1.4	-98.1 ± 1.1	TIGRE + HEROS
8580.8998	0.546	87.9 ± 1.6	-101.5 ± 0.8	TIGRE + HEROS
8583.8868	0.557	90.7 ± 1.9	-99.4 ± 0.9	TIGRE + HEROS
8595.8649	0.609	82.2 ± 1.5	-94.2 ± 1.4	TIGRE + HEROS
8620.8763	0.071	-104.3 ± 1.0	114.7 ± 2.1	TIGRE + HEROS
8622.7862	0.717	50.8 ± 0.8	-59.0 ± 1.4	TIGRE + HEROS

Table A1. continued.

HJD − 2 450 000	ϕ	RV$_P$ (km s^{-1})	RV$_S$ (km s^{-1})	Instrumentation
8623.7795	0.053	−103.4 ± 1.4	118.0 ± 0.8	TIGRE + HEROS
8625.7823	0.731	47.1 ± 1.3	−51.1 ± 1.2	TIGRE + HEROS
8626.8430	0.089	−99.6 ± 1.1	110.1 ± 3.0	TIGRE + HEROS
8943.9344	0.365	55.3 ± 1.0	−64.5 ± 1.4	TIGRE + HEROS
8953.8765	0.729	29.4 ± 1.5	−34.5 ± 1.1	TIGRE + HEROS
8962.9326	0.793	3.2 ± 1.1	−1.9 ± 1.0	TIGRE + HEROS
8971.9508	0.844	−37.4 ± 1.5	39.2 ± 0.9	TIGRE + HEROS
8981.8337	0.187	−42.2 ± 1.3	43.9 ± 1.0	TIGRE + HEROS
8990.9362	0.267	−15.5 ± 1.4	13.0 ± 1.3	TIGRE + HEROS
8994.8576	0.593	79.0 ± 1.8	−91.2 ± 2.1	TIGRE + HEROS
9000.8744	0.629	71.0 ± 1.5	−79.8 ± 1.5	TIGRE + HEROS
9014.8052	0.342	48.4 ± 1.8	−56.5 ± 1.4	TIGRE + HEROS
9035.7900	0.441	79.6 ± 2.1	−92.2 ± 1.7	TIGRE + HEROS
9045.7161	0.799	3.9 ± 1.2	−3.4 ± 0.8	TIGRE + HEROS
9297.9856	0.145	−49.8 ± 1.2	55.8 ± 0.9	TIGRE + HEROS
9311.9249	0.861	−64.5 ± 1.3	70.1 ± 1.1	TIGRE + HEROS

Column 1 gives the heliocentric Julian date (HJD) of the observations at mid-exposure. Column 2 gives the observational phase ϕ computed with the orbital period determined in Sect. 4 based on the equivalent RVs (last column in Table 4). Columns 3 and 4 give the radial velocities RV$_P$ and RV$_S$ of the primary and secondary stars, respectively. The errors represent ±1σ. Column 5 provides information about the instrumentation.

Table B1. Journal of the RVs of HD 165052 from Ferrero et al. (2013).

HJD − 2 450 000	RV$_P$ (km s^{-1})	RV$_S$ (km s^{-1})
4582.8675	98.3 ± 8.4	−106.4 ± 6.4
4693.6231	−80.9 ± 10.3	90.8 ± 11.8
4695.6483	15.6 ± 10.5	−13.2 ± 8.6
4696.5568	−83.3 ± 8.8	94.2 ± 5.6
4696.6286	−79.4 ± 7.2	93.9 ± 8.1
4696.6605	−77.3 ± 8.5	91.6 ± 6.7
4697.6220	62.9 ± 6.3	−76.0 ± 5.9
4955.8004	−7.0 ± 14.6	9.6 ± 10.6
4956.9100	−57.0 ± 8.6	62.4 ± 8.4
4964.8865	−56.1 ± 11.4	69.9 ± 8.4
4965.8323	−47.3 ± 12.0	56.7 ± 11.1
4966.8550	100.8 ± 6.2	−106.9 ± 8.4
4967.8220	−55.7 ± 14.9	65.5 ± 12.4
4968.8723	−38.3 ± 8.8	41.3 ± 6.0
5046.6533	102.5 ± 7.1	−109.5 ± 8.2
5047.7305	−67.7 ± 13.6	85.2 ± 9.4
5048.7185	−26.2 ± 9.7	30.2 ± 6.8
5049.7159	101.7 ± 10.5	−107.7 ± 5.6
5052.7320	100.1 ± 6.4	−103.5 ± 5.7
5337.6475	−94.2 ± 9.3	101.4 ± 8.5
5339.7307	44.5 ± 5.5	−50.1 ± 6.1
5340.6327	−95.7 ± 8.3	101.9 ± 11.8
5341.5812	30.4 ± 14.1	−33.0 ± 10.6
5342.6292	54.6 ± 11.7	−63.8 ± 10.2
5376.5522	−52.3 ± 12.1	59.7 ± 9.9
5378.7551	−77.5 ± 11.1	89.5 ± 9.2
5380.5253	94.3 ± 9.2	−104.5 ± 8.0
5381.7473	−82.9 ± 9.7	91.3 ± 7.0
5383.7515	90.5 ± 6.0	−97.7 ± 6.3
5429.6974	−58.2 ± 11.8	68.6 ± 7.4
5430.6168	87.2 ± 7.9	−91.1 ± 8.0
5431.6959	−42.3 ± 11.7	51.6 ± 7.5
5432.6362	−55.9 ± 10.9	69.1 ± 7.4
5433.5059	78.7 ± 11.4	−88.0 ± 7.3
5434.6834	−45.7 ± 14.0	60.3 ± 7.5
5435.5627	−64.5 ± 11.8	71.7 ± 9.3
5698.8397	−7.9 ± 9.3	41.7 ± 8.3

Column 1 gives the heliocentric Julian date (HJD) of the observations at mid-exposure. Columns 2 and 3 give the radial velocities RV$_P$ and RV$_S$ of the primary and secondary stars, respectively. The errors represent ±1σ.